Effects of CuO doping on structure, microstructure and dielectric properties of $BaTiO_3$–$PbTiO_3$ solid solution

Barbara Garbarz-Glos[a], Wojciech Bąk[a], Anna Kalvane[b], Maija Antonova[b], and Grzegorz Klimkowski[c]

[a]Institute of Technology, Pedagogical University of Cracow, Kraków, Poland; [b]Institute of Solid State Physics, University of Latvia, Riga, Latvia; [c]Faculty of Technology, Institute The Jan Grodek State Vocational Academy in Sanok, Sanok, Poland

ABSTRACT

$Ba_{0.7}Pb_{0.3}TiO_3$ and $Ba_{0.7}Pb_{0.3}TiO_3$+yCuO ($y = 0.1$ wt%, 0.5 wt%, 1 wt% and 3 wt%) samples were prepared by a solid state reaction method. High purity raw materials were used. Structural properties of the sintered pellets were studied by X-ray diffractometer X'Pert PRO (PANalytical). A single phase of perovskite structure with tetragonal phase was identified at room temperature. The surface morphology of the obtained specimens was characterized by the scanning electron microscopy (Hitachi S4700). The investigations has shown that the synthesized ceramic materials are characterized by the high density, homogeneity of microstructure and low porosity. Dielectric spectroscopy was used to study the electrical properties of the solid solution on the basis of $BaTiO_3$ doped CuO.

ARTICLE HISTORY
Received 2 October 2018
Accepted 8 February 2019

KEYWORDS
Solid solution; barium titanate; microstructure; dielectric properties

1. Introduction

The $BaTiO_3$ based compounds is one of the most favored ferroelectric oxides due to its exceptional electrical properties and finds application in ultrasonic transducers, thin-film memories and multilayer ceramic capacitors among others [1]. It was determined very early that the electrical properties of barium titanate ceramics may be changed and optimized by doping [2] (there are multiple incorporation mechanisms for dopants in the perovskite structure). The introduced cation may behave like donor if occupies Ba^{2+} site, or like an acceptor if it takes a titanium Ti^{4+} ion site [3–6]. In addition, this type of doping is also a reason of the formation of multiple defects.

Among others, the shifting of the temperature Curie point is accomplished by using of Pb^{2+} for Ba^{2+} substitution. The temperature Curie point raises monotonically at rate of 3.7 K, towards that of $PbTiO_3$, reaching the temperature of 760 K [7, 8]. The aim of this paper is to present the study of the Cu-doping influence on the structure, microstructure and electrical properties of barium lead titanate.

2. Experimental

The $Ba_{0.7}Pb_{0.3}TiO_3$ and $Ba_{0.7}Pb_{0.3}TiO_3+yCuO$ for $y = 0.05$ wt%, 0.1 wt%, 1 wt% and 3 wt% ceramics (abbreviated to 70B30PT, 70B30PT-0.05Cu, 70B30PT-0.1Cu, 70B30PT-1Cu and 70B30PT-3Cu respectively) were prepared by the solid-state reaction method using reagents: barium carbonate ($BaCO_3$), titanium dioxide (TiO_2), lead oxide (PbO) and copper oxide (CuO) as starting materials. The starting powders were weighed in accordance to the chemical formulas in case of $BaTiO_3$ and in accordance to the expected nominal compositions for $Ba_{0.7}Pb_{0.3}TiO_3$ and $Ba_{0.7}Pb_{0.3}TiO_3+yCuO$. The mixture of the raw materials was homogenized and ground in an agate ball mill in ethanol for 24 h to obtain a well-dispersed mixture. The dried material was calcined for 1–2 h at the temperature of 1323–1373 K. After calcination, the powder was ground in ethanol and cold pressed under the pressure of 100 MPa. The sintering was performed in air at the temperature range from 1473 K to 1623 K (depending on the composition) for 2 h with a heating rate of 2 K/min. To compensate for the evaporation of lead in the sintering process, 5% of PbO by weight excess was added.

The structural characteristics of all the sintered samples were determined by the X-ray diffraction (Panalytical Xpert Pro MPD diffractometer). The microstructure of the natural fracture surfaces was observed by means of high resolution scanning electron microscopy (Hitachi S4700), equipped with an Oxford Instruments Energy Dispersive X-Ray Spectroscopy (EDS) stage. All samples for the SEM/EDS analysis were cut to give cross sections and polished with abrasives. The homogeneity of element distribution in the samples was investigated by means of the EPMA method with the use of an X-ray microprobe.

The electric properties were characterized using a Novocontrol System consisting of an Alpha-AN HighPerformance Frequency Analyzer combined with Quatro Cryosystem for the temperature control and software package WinDeta. The measurements were performed in the temperature range from 173 K to 593 K, where nitrogen gas was used as a heating and cooling agent. The accuracy of the temperature stabilization was ±0.5 K. The frequencies varied from 10 Hz to 10 MHz at applied voltage 0.1 V. Prior to the electrical characterization, the pellets were polished and silver electrodes were placed on the both opposite surfaces.

3. Results

Basing on the obtained X-ray diffraction patterns (Figure 1) a phase analysis has been performed. It confirmed the mono-phase character of samples as to the chemical composition according to the assumed standards. The XRD analysis (at room temperature) revealed tetragonal phase with the P4mm space group. The obtained values of the unit cell parameters and axial ratio are given in Table 1. The slight reduction of c/a with the increase of the Cu-doping content was observed. Nevertheless, all investigated specimens showed a greater tetragonality than unity and exhibit the perovskite ABO_3 ferroelectric material structure [9].

The Table 1 also shows the sintering temperature and density for all the investigated samples. A slight decrease in density with increasing copper concentration was noticed. It is noteworthy that through the use of copper oxide as sintering additive, the

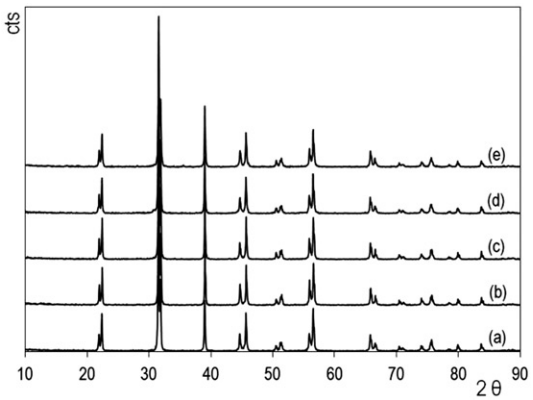

Figure 1. X-ray diffraction patterns for (a) 70B30PT; (b) 70B30PT-0.05Cu; (c) 70B30PT-0.1Cu; (d) 70B30PT-1Cu and (e) 70B30PT-3Cu samples.

Table 1. Sintering temperature for investigated samples and unit cell parameters at room temperature.

Sample	Sintering temperature [K]	Density (X-ray) [g/cm^3]	a [Å]	c [Å]	c/a ratio	V [Å^3]
70B30PT	1546	6.2233	3.87445(6)	4.05034(5)	1.04539	63.80
70B30PT-0.05Cu	1546	6.1692	3.97120(4)	4.04974(2)	1.01977	63.87
70B30PT-0.1Cu	1546	5.9883	3.97071(3)	4.05242(4)	1.02057	63.89
70B30PT-1Cu	1523	6.0874	3.97347(3)	4.04916(6)	1.01904	63.87
70B30PT-3Cu	1473	5.9909	3.97347(1)	4.04522(1)	1.01805	63.87

pronounced improvement in 70B30PT sintering was achieved. The sintering temperature for achieving the right density was lowered by 73 K. The microstructures of the obtained compositions based on $BaTiO_3$ with A-site and B-site substitution are shown in Figure 2. The images of fracture surfaces of all the investigated samples indicate the existence of the mixture of transgranular and intergranular modes of fracture. The fracture has a fragile character, and a tendency to the formation of crystalline structures can be observed in the grains. The pores have an irregular shape without curvings and narrowings. A well-developed microstructure in $BaTiO_3$ and 70B30PT samples with the integrated growth terraces of about 2.5 μm thickness was noticed. They indicate that the growth of grains took place according to the layer mechanism. These are also found in the doped ceramic. The reduction in the surface of the layered sheets is noticeable (with the distance between them preserved) as a result of a decrease in grain size of the doped ceramics. The grain size was estimated by the intercept line method. With the increase in cooper content in the investigated samples, the grains size decreases probably due to the conditions of the sintering process – the lowering of sintering temperature (the magnitude of grain size order is retained).

The Cu-distribution measured by the EPMA for the 70B30PT-3Cu is shown in Figure 3. All the samples modified with copper exhibit the expected nominal doping concentration in the grain. All the investigated samples, modified with copper exhibit the expected nominal doping concentration in the grain. In many cases an insignificant amount of the remaining dopant may be a segregated region spanning across the grain boundary. Such behavior can be related to the lower degree of solubility of Cu^{2+} ions

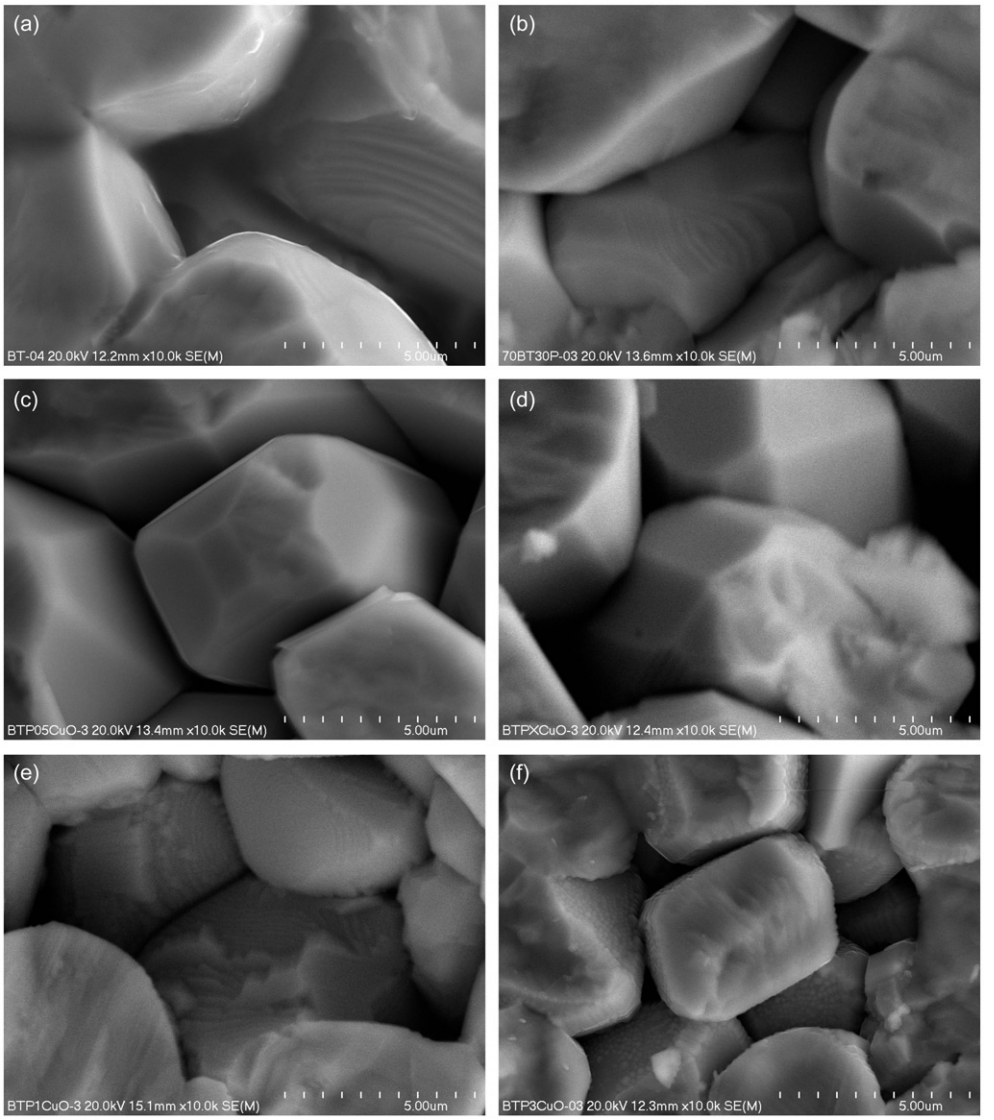

Figure 2. The SEM micrographs of the microstructure of (a) BT; (b) 70B30PT; (c) 70B30PT-0.05Cu; (d) 70B30PT-0.1Cu; (e) 70B30PT-1Cu and (f) 70B30PT-3Cu sample surface, magnified 1000×.

in $BaTiO_3$ and can be attributed to a cationic disorder due to the random distribution of B-site cations having a different ionic radius (73 pm and 60.5 pm for Cu^{2+} and Ti^{4+}, respectively).

The feature of the EPMA maps is the negligible segregation of lead at the grain boundaries, which can be linked to the A-site substitutions in the $BaTiO_3$ structure. Lead ions, due to their greater volatile, are attracted to the imperfect areas of grain boundaries during sintering, and the distribution may vary for grains (each grain developing a different strain gradients during the sintering) [10, 11]. The obtained maps of the remaining elements indicate their homogeneous chemical distribution. In the EDS survey spectrum (not shown here) nothing more than the expected elements is seen.

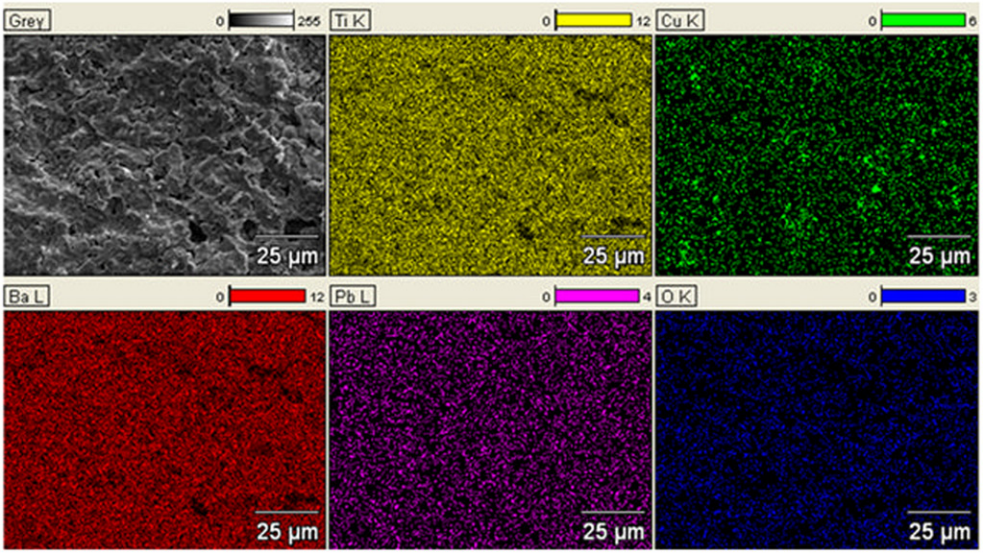

Figure 3. The photograph of the surface fragment of the 70B30PT-3Cu sample, on which the EPMA mapping was performed (magnified 1000×); the distribution of titanium, copper, barium, lead and oxygenium on the sample surface.

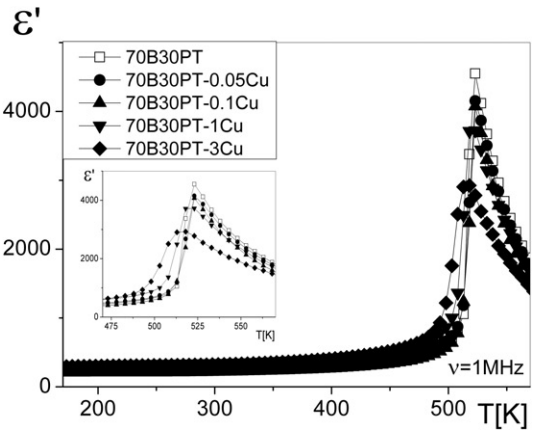

Figure 4. The temperature dependence of the real part of the complex dielectric permittivity for 70B30PT and CuO doped 70B30PT samples. The inset shows a magnified version of the selected temperature range.

Dielectric properties of all the investigated samples are shown as the temperature dependence real $\varepsilon'(T)$, (Figure 4) and imaginary $\varepsilon''(T)$, (Figure 5) parts of electric permittivity, as well as electric ac conductivity $\sigma(1/T)$, (Figure 6). The maxima of $\varepsilon'(T)$ and $\varepsilon''(T)$ seen in the Figures 4 and 5, respectively are observed at the temperatures of the paraelectric-ferroelectric phase transition. For the 70B30PT sample and those with CuO content up to 0.1 wt%, the temperature of the paraelectric-ferroelectric phase transitions is the same and equals 523 K.

On the other hand, the maximum value of $\varepsilon'(T)$ for 70B30PT-1Cu and 70B30PT-3Cu samples occurs at temperatures of 528 K and 513 K, respectively. Simultaneously with

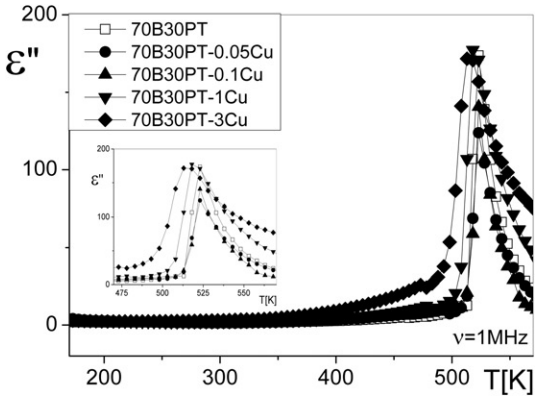

Figure 5. The temperature dependence of the imaginary part of the complex dielectric permittivity for 70B30PT and CuO doped 70B30PT samples. The inset shows magnified version of the selected temperature range.

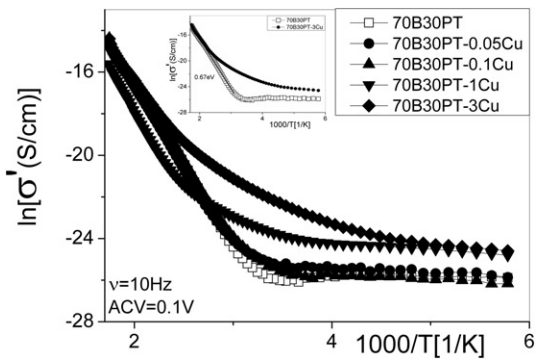

Figure 6. The temperature dependence of ac conductivity (σ') for 70B30PT and CuO doped 70B30PT samples. The inset shows magnified version for 70B30PT and 70B30PT-3Cu samples.

the increase of the CuO content in the 70B30PT solid solution, the value of maximum $\varepsilon'(T)$ decreases and the paraelectric-ferroelectric phase transition is more diffuse and broadened. Dependence of $\varepsilon''(T)$ describes the dielectric properties related to the energy loss processes of the electric field in the investigated samples. The temperature of maxima $\varepsilon''(T)$ is correlated with the maxima temperature in the graphs $\varepsilon'(T)$ and corresponds to the structural phase transitions. The dielectric losses of the investigated samples were also presented via the dependence of ac conductivity on the inverse of temperature in the so-called Arrhenius system (Figure 6).

The character of the ac conductivity plots indicates a complex mechanism of electric charge transport. The thermal activation energy determined by a linear regression method, at the frequency of measured electric field 10 Hz, is 0.67 eV (for 70B30PT sample). For the next two samples with a low content of CuO (up to 0.1 wt%), the ac conductivity mechanism is the same as for 70B30PT sample. The further increase of the CuO content in the 70B30PT solid solution enhances the ac conductivity in a low temperature range. The analysis of different theoretical models leads to the conclusion that

ac conductivity at lower temperatures originates from the migration of ions by hopping between neighboring potential wells [12, 13]. The fastest and most mobile carriers in perovskites are oxygen vacancies [14], which may be trapped by acceptor defects or can form stable pairs or larger carrier complexes [15].

4. Conclusions

The samples exhibit a crystalline perovskite structure, no formation of other phases was observed. The EDS and EPMA measurements performed in the chosen microregions during the samples surface analysis confirmed the purity and experimentally assumed qualitative and quantitative composition. Cu-doping reduced the grain sizes and led to a slight decrease in the tetragonality (c/a) of the perovskite lattice of the investigated samples. Increasing concentration of copper Cu causes the shift of the Curie temperature towards lower temperatures. It also reduces the maximum permittivity value and the paraelectric-ferroelectric phase transition is more diffuse.

References

1. K. Uchino, *Ferroelectric Devices* (CRC Press, New York, 2009).
2. F. D. Morrison, D. C. Sinclair, J. M. S. Skakle, and A. R. West, Novel doping mechanism for very-high-permittivity barium titanate ceramics, *J. Am. Ceram. Soc*. **81** (7), 1957 (2005). DOI: 10.1111/j.1151-2916.1998.tb02575.x.
3. M. Shandilya, R. Rai, and A. Zeb, Structural and dielectric relaxor properties of $Ba_{1-x}Mg_xTiO_3$ ceramics prepared through a hydrothermal route, *Adv. Appl. Ceram*. **117** (5), 255 (2018). DOI: 10.1080/17436753.2017.1405557.
4. B. Garbarz-Glos, W. Bak, M. Antonova, and M. Pawlik, Structural, microstructural and impedance spectroscopy study of functional ferroelectric ceramic materials based on barium titanate, *IOP Conf. Ser: Mater. Sci. Eng.* **49**, 012031 (2013). DOI: 10.1088/1757-899X/49/1/012031.
5. W. Smiga *et al.*, Strontium concentration dependence of selected structural and mechanical properties of $Ba_{1-x}Sr_xTiO_3$ polycrystalline, *Integr. Ferroelectr*. **108**, 77 (2009).
6. P. Dulian, W. Bąk, K. Wieczorek-Ciurowa, and C. Kajtoch, Controlled mechanochemical synthesis and properties of a selected perovskite-type electroceramics, *Mater. Sci-Pol.* **31** (3), 462 (2013). DOI: 10.2478/s13536-013-0126-4.
7. K. Suzuki, On the phase transition in barium-lead titanate, *J. Phys. Soc. Jpn*. **6** (5), 340 (1951). DOI: 10.1143/JPSJ.6.340.
8. K. M. Gupta, and N. Gupta, *Advanced Electrical and Electronics Materials: Processes and Applications. Advanced Materials Series* (Scrivener Publishing LLC and John Wiley & Sons, Massachusetts and New Jersey, 2015).
9. L. B. Kong, T. S. Zhang, J. Ma, and F. Boey, Progress in synthesis of ferroelectric ceramic materials via high-energy mechanochemical technique, *Prog. Mater. Sci*. **53** (2), 207 (2008). DOI: 10.1016/j.pmatsci.2007.05.001.
10. J. M. Holsgrove *et al.*, Mapping grain boundary heterogeneity at the nanoscale in a positive temperature coefficient of resistivity ceramic, *Apl. Mater*. **5** (6), 066105 (2017). DOI: 10.1063/1.4989396.
11. Q. Yin, B. Zhu, and H. Zeng, *Microstructure, Property and Processing of Functional Ceramics* (Metallurgical Industry Press. Springer Verlag, Berlin, 2009).
12. A. K. Jonscher, *Universal Relaxation Law* (Chelsea Dielectric Press, London, 1996).
13. K. L. Ngai, Analysis of NMR and conductivity-relaxation measurements in glassy Li2S-SiS2 fast-ion conductors. *Phys. Rev., B Condens. Matter*. **48** (18), 13481 (1993).

14. N. Sareecha *et al.*, Fabrication and electrical investigations of Pb-doped $BaTiO_3$ ceramics, *Mater Chem Phys*. **193**, 42 (2017). DOI: 10.1016/j.matchemphys.2017.01.088.
15. F. Cordero, F. Craciun, and F. Trequattrini, Ionic mobility and phase transitions in perovskite oxides for energy application, *Challenges*. **8** (1), 5 (2017). DOI: 10.3390/challe8010005.

Institute of Solid State Physics, University of Latvia as the Center of Excellence has received funding from the European Union's Horizon 2020 Framework Programme H2020-WIDESPREAD-01-2016-2017-TeamingPhase2 under grant agreement No. 739508, project CAMART²